

Improvements in the X-Ray Analytical Capabilities of a Scanning Transmission Electron Microscope by Spherical-Aberration Correction

M. Watanabe,^{1,*} D.W. Ackland,¹ A. Burrows,¹ C.J. Kiely,¹ D.B. Williams,¹ O.L. Krivanek,² N. Dellby,² M.F. Murfitt,² and Z. Szilagy²

¹Department of Materials Science and Engineering/Center for Advanced Materials and Nanotechnology, Lehigh University, Bethlehem, PA 18015, USA

²NION Co., Kirkland, WA 98033, USA

Abstract: A Nion spherical-aberration (Cs) corrector was recently installed on Lehigh University's 300-keV cold field-emission gun (FEG) Vacuum Generators HB 603 dedicated scanning transmission electron microscope (STEM), optimized for X-ray analysis of thin specimens. In this article, the impact of the Cs-corrector on X-ray analysis is theoretically evaluated, in terms of expected improvements in spatial resolution and analytical sensitivity, and the calculations are compared with initial experimental results. Finally, the possibilities of atomic-column X-ray analysis in a Cs-corrected STEM are discussed.

Key words: spherical-aberration corrector (Cs-corrector), probe formation, spatial resolution, minimum mass fraction, minimum detectable mass, quantitative thin-film X-ray analysis, ζ (zeta)-factor method, grain-boundary segregation

INTRODUCTION

Spherical aberration (Cs) is a major electron-lens defect and has been the dominant limiting factor since the transmission electron microscope (TEM) was originally developed. Cs considerably degrades the image resolution in TEM and fine probe formation in STEMs. Because the Cs-limited resolution is proportional to the term $(C_s \lambda^3)^{1/4}$ (where C_s is the spherical-aberration coefficient and λ is the electron wavelength), TEM manufacturers have historically developed higher-voltage (i.e., smaller λ) instruments to minimize the influence of the spherical aberration. Despite significant efforts to correct Cs, this had not been very successful until the last decade due to many practical difficulties, as reviewed by Hawkes and Kasper (1996).

In the last decade, three different types of Cs-correctors were developed: (1) quadrupole-octupole coupled lenses to correct both spherical and chromatic aberrations for lower-voltage scanning electron microscopes (Zach & Haider, 1995), (2) a Cs-corrector consisting of hexapoles and transfer lenses for TEMs and STEMs by Haider and coworkers (Haider et al., 1998a; Sawada et al., 2005) based on the concepts originally proposed by Rose (1990), and (3) a quadrupole-octupole coupled Cs-corrector for VG dedi-

cated STEMs by Krivanek and coworkers (Krivanek et al., 1999). Using the TEM Cs-corrector, the contrast delocalization effect can be significantly minimized (Haider et al., 1998b), and the contrast of oxygen-atom columns in ceramic-oxide specimens can be enhanced by tuning C_s to negative values (Jia et al., 2003) for atomic-resolution, phase-contrast imaging. Conversely, the STEM Cs-corrector can refine the incident probe dimensions significantly and the resolution in high-angle annular dark-field (HAADF) STEM imaging can reach ~ 1 Å and ~ 0.6 Å levels in 120- and 300-keV instruments, respectively (Batson et al., 2002; Nellist et al., 2004). In addition, materials characterization at the atomic level can routinely be performed by electron energy-loss spectrometry (EELS) in a Cs-corrected STEM (e.g., Varela et al., 2005). However, no practical investigation has yet been reported about the benefits of Cs correction for (S)TEM X-ray analysis.

The probe refinements by the Cs correction can be very useful for X-ray energy dispersive spectrometry (XEDS). At Lehigh University, the STEM Cs-corrector produced by Nion (Krivanek et al., 2003) was recently installed on a Vacuum Generators HB 603 dedicated STEM. This instrument was designed to provide maximum X-ray analysis performance (Lyman et al., 1994): a 300-keV cold FEG with a brightness of 10^{13} Am⁻²sr⁻¹ giving a high beam current (~ 1.0 nA) in a 1.5-nm probe at full-width tenth-maximum (FWTM), an optimum pole-piece designed to give two XEDS detectors the highest possible collection angle (0.3 sr

for a detector with a 30-mm² active area), a column designed to minimize stray electrons and X-rays, and a specimen stage lined with Be to enhance the X-ray peak-to-background ratio (>6000 for a pure Cr film at 300 keV, and an ultrahigh vacuum $<10^{-7}$ Pa in the stage and $<10^{-9}$ Pa at the gun). The details of the design concepts can be found in the original paper (Lyman et al., 1994). The HB 603 at Lehigh already produces the best thin-foil X-ray analysis capability in the world: Analysis can be routinely performed with a spatial resolution in the range of 2–3 nm (Keast & Williams, 1999; Williams et al., 2002) and an analytical sensitivity approaching 2–3 atoms in a homogeneous solid-solution alloy (Watanabe & Williams, 1999a). In addition, the extraordinary stage stability of the HB 603 (>0.1 nm/min specimen drift) makes it possible to apply high-resolution X-ray mapping to detect ultrafine features in materials, such as grain-boundary (GB) segregation (e.g., Keast & Williams, 1999; Watanabe & Williams, 2003) and nanoscale precipitates/particles (e.g., Rodríguez-González et al., 2005; Burke et al., 2006). The combination of the HB 603 and the Nion corrector is expected to further improve these performance figures approaching atomic-column spatial resolution and single-atom detection sensitivity.

In this article, therefore, the impact of the Cs-corrector on X-ray analytical performance is first evaluated theoretically in terms of spatial resolution and analytical sensitivity. Second, the first results generated by the HB 603 after installation of the Nion corrector are described. Finally, the possibilities of atomic-column X-ray analysis in a Cs-corrected STEM are discussed.

THE NION CS-CORRECTOR SYSTEM

Nion initially developed a Cs-corrector for VG dedicated STEMs (Krivanek et al., 1999) and improved its design to reduce the total chromatic aberration introduced by the Cs-corrector and to further improve the stability (Dellby et al., 2001; Krivanek et al., 2003). The second-generation corrector has been commercialized and installed on several VG STEMs. Image resolutions of <1 Å and <0.7 Å can be achieved for 100- and 300-keV instruments, respectively (e.g., Batson et al., 2002; Nellist et al., 2004). The second-generation version was also installed on the HB 603 STEM at Lehigh by retrofitting in the column where the VG scan coils were originally located. This particular corrector consists of four quadrupoles and three octupoles, numerous auxiliary alignment and adjustment coils, and power supplies (Krivanek et al., 2003). In addition, the Nion corrector requires a fiber-optically coupled CCD camera to record defocused shadow images (Ronchigrams) for tuning the various lens parameters of the corrector. During the corrector installation, a $1\text{ k} \times 1\text{ k}$ CCD camera was also mounted after the postspecimen lenses. In the Nion system, the alignment of the corrector lenses can be performed by

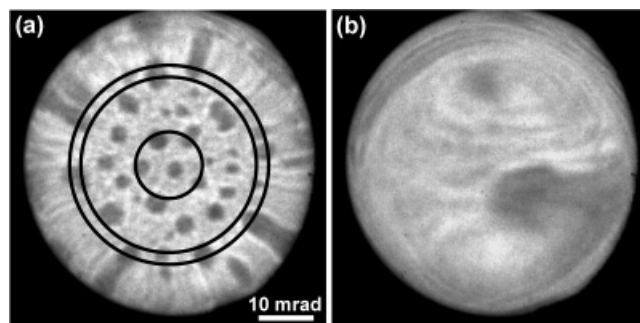


Figure 1. Ronchigrams (defocused shadow images) recorded in the HB 603 from a specimen of Au particles on a carbon film at defocus values of -800 nm (a) and -10 nm (b) after tuning the Cs-corrector. The radii of the three circles in a indicate 6, 15, and 17 mrad. After installing the corrector, the uniform-intensity area in the Ronchigram is expanded up to 17 mrad as shown in b, compared with 6 mrad in the uncorrected HB 603 column.

measuring displacements of some specimen features in multiple Ronchigrams, from which all axial aberrations up to fifth order can be measured and the aberrations up to third order can automatically be adjusted to the optimum conditions (Dellby et al., 2001).

Figure 1 shows typical Ronchigrams at the defocus values of -800 nm (a) and -10 nm (b) taken from a carbon film with Au particles, after tuning the corrector in the HB 603. As shown in the defocused Ronchigram (Fig. 1a), the image of the Au particles is not distorted up to a semiangle of 17 mrad, drawn as the largest circle. In the Ronchigram near the appropriate focus (Fig. 1b), the intensity distribution is uniform within 17 mrad, in which the aberration of the lenses no longer influences the probe formation. After this tuning, C_s becomes -0.16 mm with the fifth-order aberration coefficient (C_5) of 500 mm. The inherent C_s value of the objective lens in the HB 603 is very high (4.3 mm) due to the large pole-piece gap, designed thus to maximize the X-ray collection angle. The smallest circle drawn in Figure 1a represents the aberration-free region (6 mrad) in the original HB 603. With the Cs-corrector, the aberration-free area is expanded by a factor of three. The middle circle in Figure 1a indicates the optimum aperture size currently available that provides a semiangle of 15 mrad. It should be mentioned that C_5 is the dominant coefficient limiting the aberration-free region in the current Cs-corrected condition.

THEORETICAL EVALUATION OF IMPACTS OF X-RAY ANALYSIS IN A CS-CORRECTED INSTRUMENT

Theoretical and experimental studies have proven that HAADF imaging and atomic-scale EELS analysis are signif-

icantly improved by the STEM C_s correction (e.g., Varela et al., 2005). In this section, theoretical aspects of X-ray analysis in C_s -corrected STEMs are described in terms of spatial resolution and detectability limit.

Probe Sizes

Simulated incident electron distributions and probe sizes were used to calculate the resolution approachable in C_s -corrected STEMs (e.g., Krivanek et al., 1999; Haider et al., 2000). Most of the previous studies focused mainly on the ultimate resolution achievable in C_s -corrected HAADF-STEMs imaging and typically did not consider any contribution of the electron current to the probe formation. Because atomic resolution HAADF images are usually acquired with a limited probe current (e.g., >10 pA) in conventional STEMs, the contribution of the probe current may not be important. However, one of the major differences between HAADF imaging and X-ray analysis is the need for sufficiently high probe currents to generate sufficient X-ray counts for quantification. Both X-ray generation and X-ray collection are relatively poor in STEMs. Therefore, the contribution of the probe current must be taken into account when discussing the spatial resolution for analysis, as originally pointed out by Brown (1981). The contribution of the probe current can be described as an initial Gaussian diameter of the electron gun. In this study, probe sizes were simulated by convolution of the monochromatic intensity distribution calculated by the wave-optical treatment with the Gaussian image of the electron gun (Colliex & Mory, 1984; Mory et al., 1985).

Figure 2 shows the simulated probe sizes (FWTM) with the probe current (I_p) of 0.5 nA in both the uncorrected (closed circle) and C_s -corrected (open circle) conditions of the HB 603, plotted as a function of the convergence semi-angle (α). There are several definitions of the probe size and the probe diameter and the full width at half maximum (FWHM) is commonly used when defining the image resolution. Recently, Haider et al. (2000) employed the probe diameter containing 59% of the total intensity to discuss the resolution in HAADF STEM imaging. However, the FWTM probe size is a more relevant description for analysis, because 90% of the total intensity is contained in the FWTM diameter, and X-rays are generated from the full probe-specimen interaction volume. In addition, the spatial resolution for analysis can consistently be converted from the FWTM probe size (Reed, 1982; Michael et al., 1990; Williams et al., 1992).

In both the uncorrected and C_s -corrected conditions, the probe size becomes a minimum (optimum) at a specific convergence semiangle, as shown in Figure 2. In the uncorrected condition with $C_s = 4.3$ mm, the optimum probe size is ~ 1.1 nm with $I_p = 0.5$ nA at $\alpha = \sim 6$ mrad and a defocus (Δz) of -100 nm. In contrast, the optimum probe size can be as small as 0.35 nm at 17 mrad in the C_s -corrected condition with $C_s = -0.16$ mm, $C_5 = 500$ mm, and $\Delta z =$

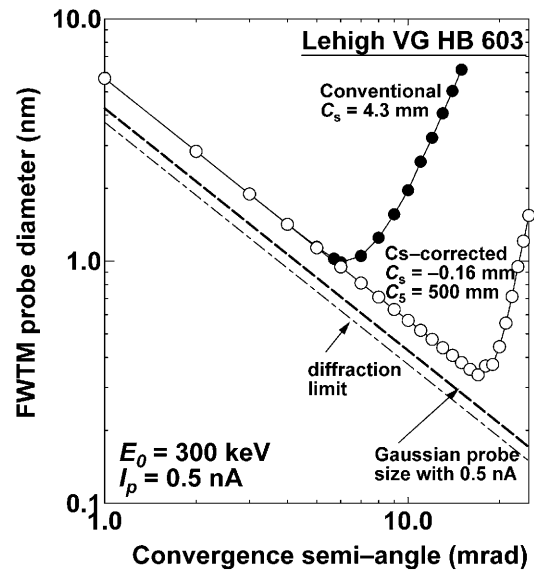


Figure 2. The simulated FWTM probe size with a beam current of 0.5 nA in the uncorrected (closed circle: $C_s = 4.3$ mm) and C_s -corrected (open circle: $C_s = -0.16$ mm, $C_5 = 500$ mm) HB 603 (300 keV), plotted against the convergence semiangle. When the Nion C_s -corrector is used, the optimum angle is shifted from 6 mrad to 17 mrad, as the Ronchigrams (Fig. 1) indicate.

-13 nm while maintaining the same probe current. These aberration coefficients in the C_s -corrected condition were measured after tuning the corrector as described above. The shift of the optimum condition to higher α by the C_s -corrector is very important for analysis because the Gaussian-probe term (shown as a dashed line in Fig. 2) decreases as α increases. So, the contribution of the Gaussian probe becomes marginal at the higher α range because the large aperture allows the source to be more greatly demagnified for the same beam current and then the smallest probe can be obtained with the highest probe current (which is the essential requirement for X-ray analysis) by means of the C_s -corrector. The higher optimum angle may also provide advantages in EELS analysis because the delocalization effects due to inelastic scattering can be reduced at higher α (Pennycook, 1982). It should be mentioned that the slope of the probe-size plot in the region above the optimum angle in the C_s -corrected condition is steeper than that in the uncorrected condition. This difference in the slopes implies that the fifth-order aberration (instead of the third-order) indeed becomes dominant at higher convergence angles in the C_s -corrected condition.

Figure 3 shows three simulated intensity distributions for incident probes with $I_p = 0.5$ nA: the optimum probe in the uncorrected condition (a), the probes at 15 mrad (b), and 17 mrad (c) in the C_s -corrected condition. As mentioned above, 15 mrad is the optimum aperture size currently available in the HB 603 at Lehigh. So, the intensity distribution shown in Figure 3b is the current best probe

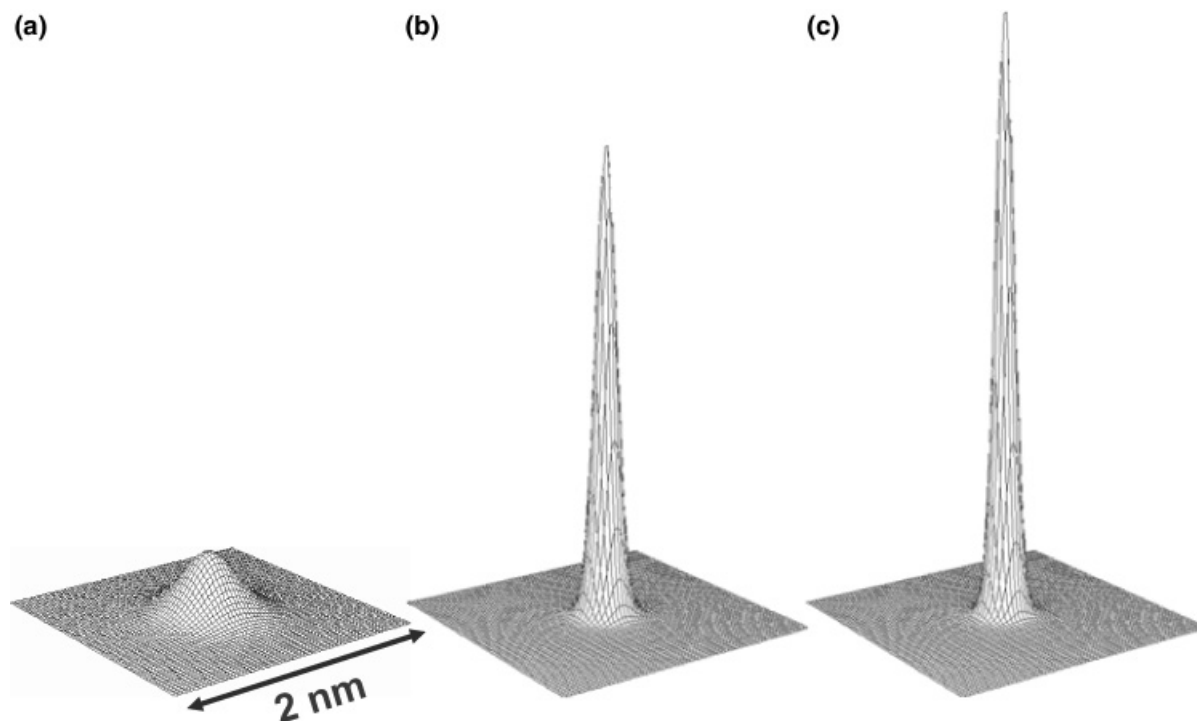


Figure 3. The simulated intensity distribution of the incident probes containing a current of 0.5 nA: (a) the uncorrected HB 603 provides a 1.1 nm probe (FWTM) with $C_s = 4.3$ mm, $\alpha = 6$ mrad, and $\Delta z = -100$ nm, (b) the C_s -corrected HB 603 with the best currently available aperture (0.4 nm at $\alpha = 15$ mrad), and (c) the optimum probe in the C_s -corrected HB 603 (0.35 nm at $\alpha = 17$ mrad). For simulation of the probes in the C_s -corrected HB 603, the following parameters were used: $C_s = -0.16$ mm, $C_5 = 500$ mm, and $\Delta z = -13$ nm.

that still provides 0.5 nA in a 0.4 nm (FWTM) probe with $\Delta z = -13$ nm. After C_s correction, the incident probe size is refined by a factor of ~ 2.5 (i.e., from 1.1 to 0.4 nm) while maintaining the same beam current (0.5 nA). Furthermore, the peak intensities of the C_s -corrected probes at 15 and 17 mrad are enhanced, compared with the conventional probe, by factors of 7.5 and 9.5, respectively. This enhancement may provide a better signal-to-noise ratio in imaging. It is important to note that a C_s -corrector corrects the lens aberration only, and has no effect on the microscope instabilities or chromatic aberration. Fortunately, the cold FEG in the HB 603 (which is consistently able to provide an energy spread < 0.5 eV) and the high operating voltage (300 keV) minimize the chromatic aberration.

Spatial Resolution

The incident beam size is the primary limiting factor for the spatial resolution of X-ray analysis if very thin specimens (≥ 50 nm) are examined. The spatial resolution can ultimately approach the incident probe size. The best results to date, in the uncorrected condition, demonstrated that atomically discrete compositional changes across an edge-on γ'/α interface in a Ni-Al-Mo alloy in a 30-nm-thick specimen can be measured within 2.4 nm (FWTM) (Williams

et al., 2002). This situation represents the best achievable spatial resolution of X-ray analysis in the uncorrected STEM.

The spatial resolution of X-ray analysis can be estimated for thin specimens of amorphous or crystalline materials, which are not oriented close to any symmetric zone axes, by using the Gaussian beam-broadening model (Doig & Flewitt, 1982; Van Cappellan & Schmitz, 1992). Figure 4 shows the spatial resolution (FWTM) calculated for a Cu thin specimen in the uncorrected and C_s -corrected conditions, plotted against the specimen thickness. Obviously, a finer probe size provides better spatial resolution. In the C_s -corrected HB 603, the spatial resolution can be kept below 1 nm for specimen thicknesses up to 40 nm. More importantly, the spatial resolution of X-ray analysis can reach atomic dimensions below thicknesses of 20 nm, which makes X-ray analysis competitive with EELS in terms of spatial resolution (Batson, 1995; Browning & Pennycook, 1995).

Analytical Sensitivity

The best analytical sensitivity achieved in the uncorrected HB 603 was the detection of ~ 0.12 wt% Mn in a 15-nm-thick specimen of a Cu-Mn alloy, which corresponds to 2–3 Mn atoms in the analysis volume (Watanabe & Williams,

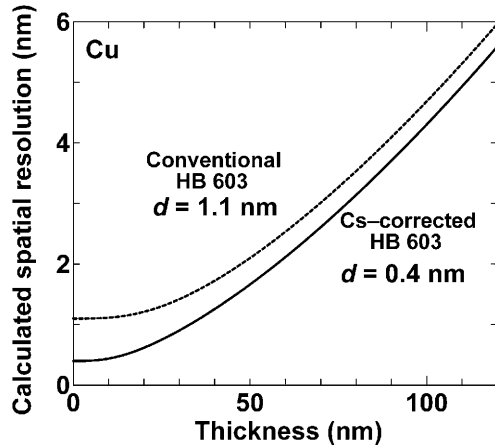


Figure 4. Comparison of the simulated spatial resolution (FWTM) of X-ray analysis of Cu in the uncorrected and Cs-corrected HB 603, plotted against the specimen thickness. The spatial resolution can be kept <1 nm for specimen thicknesses up to 40 nm.

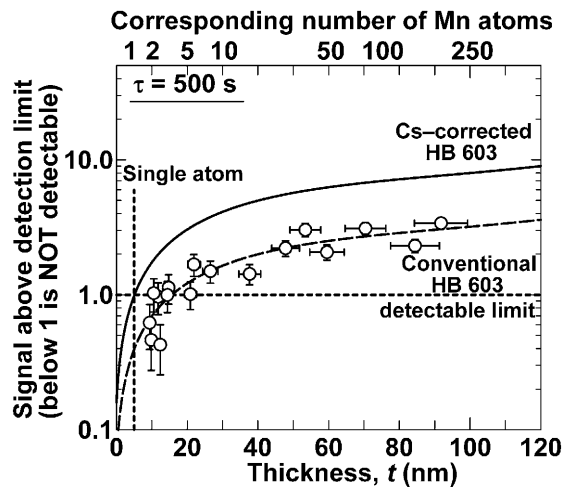


Figure 5. The detection limit of Mn atoms in a thin foil of Cu-0.12 wt% Mn solid solution, obtained in the uncorrected HB 603 indicated as closed circles, modified from Watanabe and Williams (1999a). Under these conditions ~2 Mn atoms are detectable in a 15-nm-thick region. The solid line indicates the detection limit calculated with the same probe size (1.1 nm) and a 10× higher probe current in the Cs-corrected 603. The detection limit (MMF) using the Cs-corrected probe can be ~3× better than for the uncorrected HB 603 for the same acquisition conditions.

1999a). These experimental results on the detectability measurements are shown as closed circles in Figure 5. In this plot, the vertical axis is the ratio of the measured Mn $K\alpha$ characteristic-peak X-ray intensity to the minimum-required intensity for the detection of the peak, estimated from the corresponding background intensity (Romig & Goldstein, 1979). So, if the ratio exceeds one (drawn as a dashed line),

the peak intensity is detectable with a 99% confidence limit (3σ) in this case. The details of this plot can be found in a previous paper (Watanabe & Williams, 1999a).

In analytical techniques, the smallest detectable concentration and the minimum number of detectable atoms are usually defined as the minimum mass fraction (MMF) and the minimum detectable mass (MDM), respectively (Joy & Maher, 1977). The MMF can be expressed as (Ziebold, 1967)

$$MMF \propto \frac{1}{\sqrt{P(P/B)\tau}}, \quad (1)$$

where P is the X-ray peak intensity, B is the background intensity, and τ is the acquisition time. To improve the MMF, all three factors P , P/B , and τ need to increase. In the Cs-corrected condition, similar peak intensities can be gathered because the probe current is not degraded by the Cs correction despite the formation of much smaller probes. Therefore, the MMF in the Cs-corrected condition should remain at levels similar to the uncorrected condition, unless P/B is degraded due to the installation of the Cs-corrector. Conversely, the analysis volume is significantly reduced in the Cs-corrected condition due to the smaller probe, and hence the MDM, in terms of a number of atoms, should be reduced. For example, the number of atoms in the analysis volume with the Cs-corrected probe can be reduced to ~20% of that obtained with the uncorrected probe in a 15-nm-thick specimen. Therefore, the MDM can be improved by factors from 2 to 5, that is, the single-atom detection is feasible using the HB 603 when combined with the Cs-corrector. In this condition, MMF would slightly be degraded due to the improved analyzed volume. However, the degradation is marginal because the same levels of the probe current can be applied.

In addition, more probe current can be added into the Cs-corrected probe to achieve the same probe size as that in the uncorrected condition. In Figure 6, the optimum probe sizes at FWTM in both the uncorrected and Cs-corrected conditions are plotted against the probe current. These probe sizes were simulated in the same manner as those in Figure 2. In the Cs-corrected condition, the probe current can be increased to ~6.0 nA to form a 1.1-nm probe, which is equivalent to the uncorrected probe size containing 0.5 nA. Thus a >10× higher current can be used in the Cs-corrected condition compared with the uncorrected condition. The MMF calculated with the 10× higher current is plotted as a solid line in Figure 5. Clearly, the MMF can be ~3× better for the same acquisition conditions, which also ensures single-atom detection in the Cs-corrected HB 603. Note that no conventional Si(Li) XEDS detector can deal with the higher X-ray intensity generated with the 10× current because of the limit in throughput of X-ray acquisition (at most a few kcps). However, this situation can be offset by employing a recently developed silicon-drift detec-

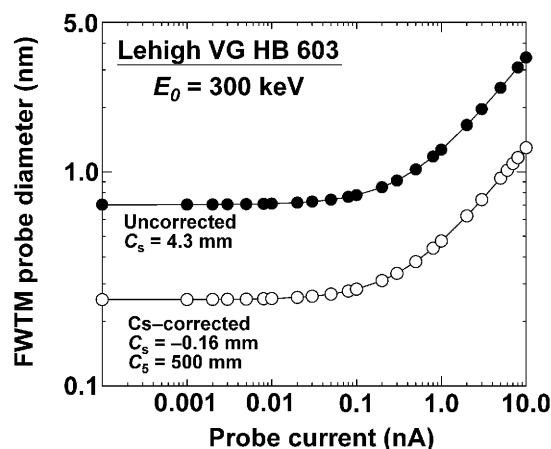


Figure 6. The simulated FWTM probe-size in the uncorrected (closed circle: $C_s = 4.3$ mm and $\alpha = 6$ mrad) and Cs-corrected (open circle: $C_s = -0.16$ mm, $C_s = 500$ mm, and $\alpha = 15$ mrad) HB 603 (300 keV), plotted against the probe current. Note that the probe size is almost independent of the probe current up to 0.1 nA for both the uncorrected and Cs-corrected conditions.

tor (SDD), with which X-rays can be gathered at count rates >100 kcps, as reported by Newbury (2005). At this moment, the SDD is not commercially available for a STEM. However, it has been tested in STEM (Zaluzec, 2004), and is, therefore, a promising candidate for Cs-corrected STEMs generating much higher beam currents.

EXPERIMENTAL RESULTS AND DISCUSSION

Preliminary Test for XEDS Performance after Corrector Installation

It is always wise to perform fundamental tests after a major modification to any instrument. In this study, a “hole-count” test was performed using a NiOx standard thin film on a Mo grid (Egerton & Cheng, 1994; Bennett & Egerton, 1995) to check for any major differences in X-ray spectra before and after the Cs-corrector installation. Figure 7 shows X-ray spectra taken from the NiOx thin film in the HB 603 with a probe current of 0.5 nA before and after the Cs-corrector installation. These spectra are identical. The inverse hole count, defined as the ratio of the Ni $K\alpha$ to the Mo $K\alpha$ lines, which describes the magnitude of spurious X-rays in the microscope column (Lyman & Ackland, 1991), was determined from 20 spectra in each of the conditions. The inverse hole-count values before and after installation are 53.6 ± 5.5 and 53.8 ± 6.8 , respectively. In addition, the P/B ratios determined at the Ni $K\alpha$ peak using the Fiori definition (Fiori et al., 1982) are 3200 ± 400 and 3500 ± 500 in the conventional and the Cs-corrected conditions, respectively. Because no significant difference was found in the

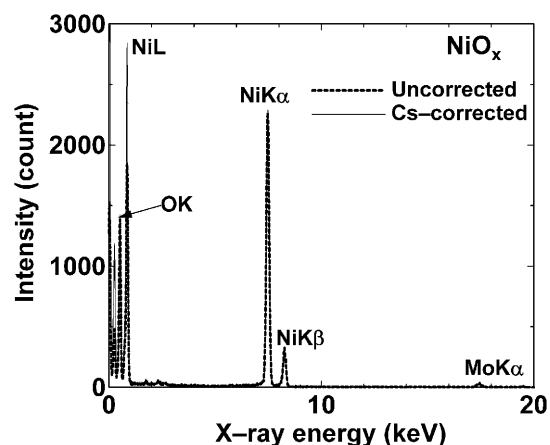


Figure 7. Comparison of X-ray spectra taken from NiOx thin film before and after the Cs-corrector installation.

XEDS performance before and after the corrector installation, the MMF should remain similar, as deduced above.

Quantitative X-ray Spectrum Imaging in the Cs-Corrected HB 603

In the Cs-corrected HB 603, X-ray spectrum imaging was performed around a GB in a Ni-base alloy. An ADF-STEM image around the GB is shown in Figure 8a. The X-ray spectrum image with 64×64 pixels and 1024 energy channels was acquired with a dwell time of 200 ms/pixel from the square region in the figure, the lower part of which is the GB between two γ grains, and the upper portion of which is the interphase interface between the γ grain at the top-left corner and a coarse γ' precipitate at the top right. The length of each field of view is 25 nm. The composition maps of major components in this alloy are also shown in Figure 8: Cr (b), Fe (c), Ti (d), and Al (e). For quantification, the ζ -factor method (Watanabe & Williams, 1999b, 2003, 2006) was applied. Composition profiles of Cr, Fe, and Ti across the γ/γ' interface region on the GB are shown in Figure 9a. These profiles are extracted from the composition maps by binning 20 pixels, which correspond to a 4-s acquisition at each analysis point. The error bar indicates a 99% confidence limit (3σ). The spatial resolution estimated from the profiles is ~ 1.8 nm in FWTM. By applying the ζ -factor method, specimen thickness can also be determined from the X-ray intensities, and hence the spatial resolution at any analyzed point can be estimated (Watanabe & Williams, 2003, 2006). In Figure 9, the specimen-thickness (b) and spatial-resolution (c) maps are also shown. For the estimation of the spatial resolution, the Gaussian beam-broadening model (Doig & Flewitt, 1982; Van Cappellan & Schmitz, 1992) was used. Around the GB area, the specimen thickness is ~ 60 nm and the estimated spatial resolution is <2 nm, which is comparable with the measurement from the profiles. Using the Cs-corrected probe, spa-

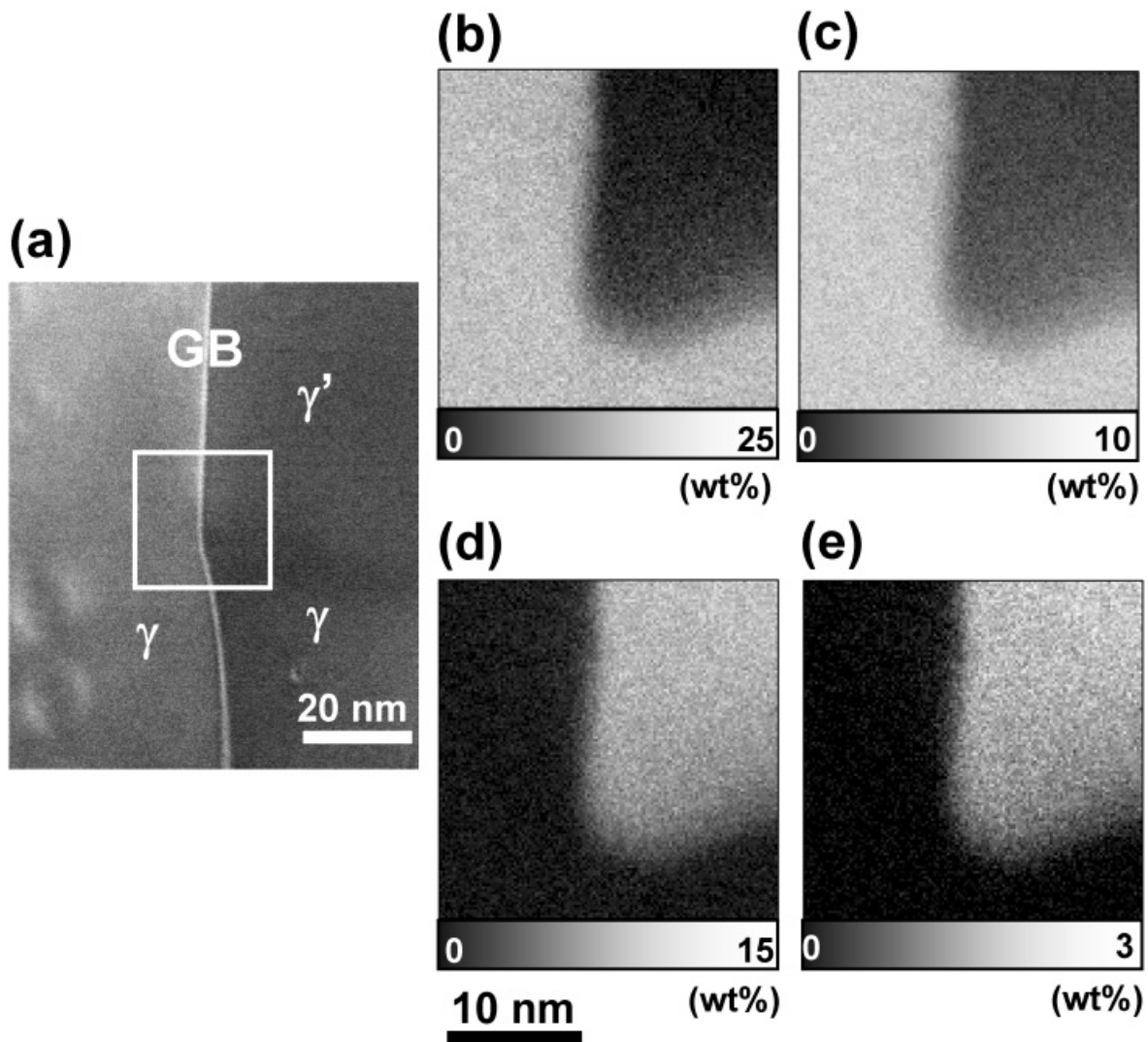


Figure 8. A series of composition maps around a GB in a Ni-base alloy measured by XEDS in the Cs-corrected HB 603 STEM. These maps were quantified by the ζ -factor method. **a:** ADF-STEM image, **b:** Cr map, **c:** Fe map, **d:** Ti map, and **e:** Al map.

tial resolution <2 nm is achievable as calculated in the previous section.

Further analysis was performed on the X-ray spectrum image by applying principal component analysis (PCA). PCA is one of several multivariate statistical analysis (MSA) techniques that can be used to identify any statistically significant features in large data sets such as spectrum images and to reduce random-noise components efficiently in a statistical manner (e.g., Jolliffe, 2002; Malinowski, 2002). A loading spectrum and the associated score image of one of components extracted from the spectrum image by PCA are shown in Figure 10a,b, respectively. The loading spectrum describes a specific spectral feature deviated from the average and the score image represents the spatial amplitude of the loading spectrum. Because PCA can extract only abstract components, which do not represent easily inter-

pretable information but simply indicate deviations from the average, there are both positive (K and L peaks of Zr and Nb) and negative (K peaks of Ti, Cr, Ni) peaks in the loading spectrum. These positive and negative peaks are enhanced in the score image. The brighter region in the score image corresponds to the GB; thus, the PCA indicates that Zr and Nb cosegregate at the GB. The composition maps of Nb and Zr quantified after the PCA noise reduction are shown in Figure 10c,d. Zr is present at a nominal 0.04 wt% (well below the detection limit), so it has not been quantified or mapped previously in this alloy via STEM-XEDS. Likewise, the amount of Nb remaining for subsequent intergranular segregation is at trace levels because the nominal amount of Nb is also low (<1 wt%) and it is known that Nb is associated with γ' precipitates and carbides in this alloy (Miller & Burke, 1993). To the authors'

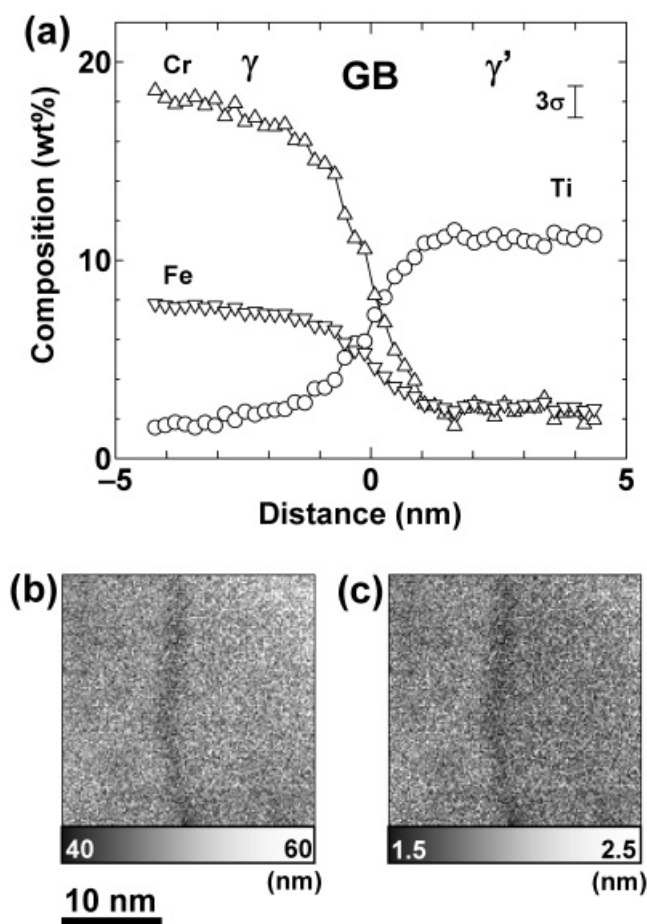


Figure 9. Composition profiles of Cr, Fe, and Ti across the γ/γ' interphase interface region on the GB extracted from the composition maps (Fig. 8) by binning 20 pixels along a line across the interface to improve counting statistics (a). The error bar indicates a 99% confidence level (3σ). Thickness map (b) and spatial resolution map (c) determined from the same field of view as shown in Figure 8 by the ζ -factor method.

knowledge, there is no report of GB segregation of either Zr or Nb in this alloy. Figure 11 shows composition profiles of Zr across the γ/γ' interface region (a) and the noninterphase region (b) on the GB, respectively, extracted from the map again by binning 20 pixels along the interface and the GB to improve counting statistics. The error bar represents a 99% confidence limit (3σ). The error levels are higher than those in Figure 9 due to the limited statistical accuracy of the low X-ray intensities (because of the shorter acquisition time and much lower composition of the alloying elements), but the Zr composition at the GB can still be clearly distinguished from that within the grains. The spatial resolutions determined from these segregation profiles are ~ 0.4 – 0.6 nm (FWTM). This is the best spatial resolution that has ever been obtained in X-ray analysis. It should be noted that the spatial resolution measured from these segregation profiles is better than that from the profiles

across the γ/γ' interface region as shown in Figure 9a. The difference in spatial resolution may be caused by the limited statistics in the Zr segregation profiles. If the errors of Zr compositions are taken into account, the spatial resolution of the segregation profile is degraded to ~ 1.5 nm, which, nevertheless, is a substantial improvement on uncorrected data.

Maps of the Zr enrichment and the number of Zr atoms calculated from a combination of the Zr composition and thickness maps are shown in Figure 10e,f. The method of extracting this information can be found in the previous papers (Watanabe & Williams, 1999b, 2003, 2006). The Zr enrichment on the GB is ~ 2 – 3 atoms/nm² obtained from the enrichment map, which corresponds to 0.12–0.17 monolayer (based on the atomic density of the close-packed (111) plane in this alloy). As shown in Figure 10f, the enrichment amounts to only 20–40 Zr atoms at both the γ/γ' interface and the GB regions. The Cs-corrected probe could focus on the limited amounts of Zr atoms in the GB. In other words, such small clusters of atoms highly localized in limited regions may be simply invisible to the relatively larger probe with higher probe currents in the uncorrected condition. Therefore, not only spatial resolution but also MDM is significantly improved, as calculated in the previous section. These are encouraging facts because hitherto unsuspected details of elemental distributions may now be characterized in the AEM because of the superior quantification, analytical sensitivity, and spatial resolution, all improved by a combination of the ζ -factor method, spectrum imaging, PCA, and Cs-correction techniques.

Toward Atomic-Column X-Ray Analysis

Atomic-column EELS analysis has routinely been performed both in uncorrected and Cs-corrected STEMs (Battson, 1995; Browning & Pennycook, 1995; Varela et al., 2005). For X-ray analysis, such atomic-column spectrum acquisition has not even been attempted because atomic-resolution STEM images are not obtainable with the higher probe currents (and consequent large probes) required for X-ray analysis in conventional STEMs. Because the Cs-corrector makes it possible to reduce the incident probe size while maintaining higher currents, however, it may be feasible to perform atomic-column X-ray analysis. Figure 12 shows a HAADF-STEM image taken from a ZrO₂ (110) thin specimen in the Cs-corrected HB 603 with a current of 0.5 nA (the X-ray analysis condition). The atomic column positions are barely resolved. The atomic positions can be extracted from the fast-Fourier transformed (FFT) image added at the left bottom corner in Figure 12. Obviously there is no comparison with most other HAADF images in Cs-corrected STEMs. However, this image was taken in the Lehigh HB 603 with a large pole-piece gap (9 mm), originally designed to insert the XEDS detectors into the column as close to the specimen as possible. So, this image is the

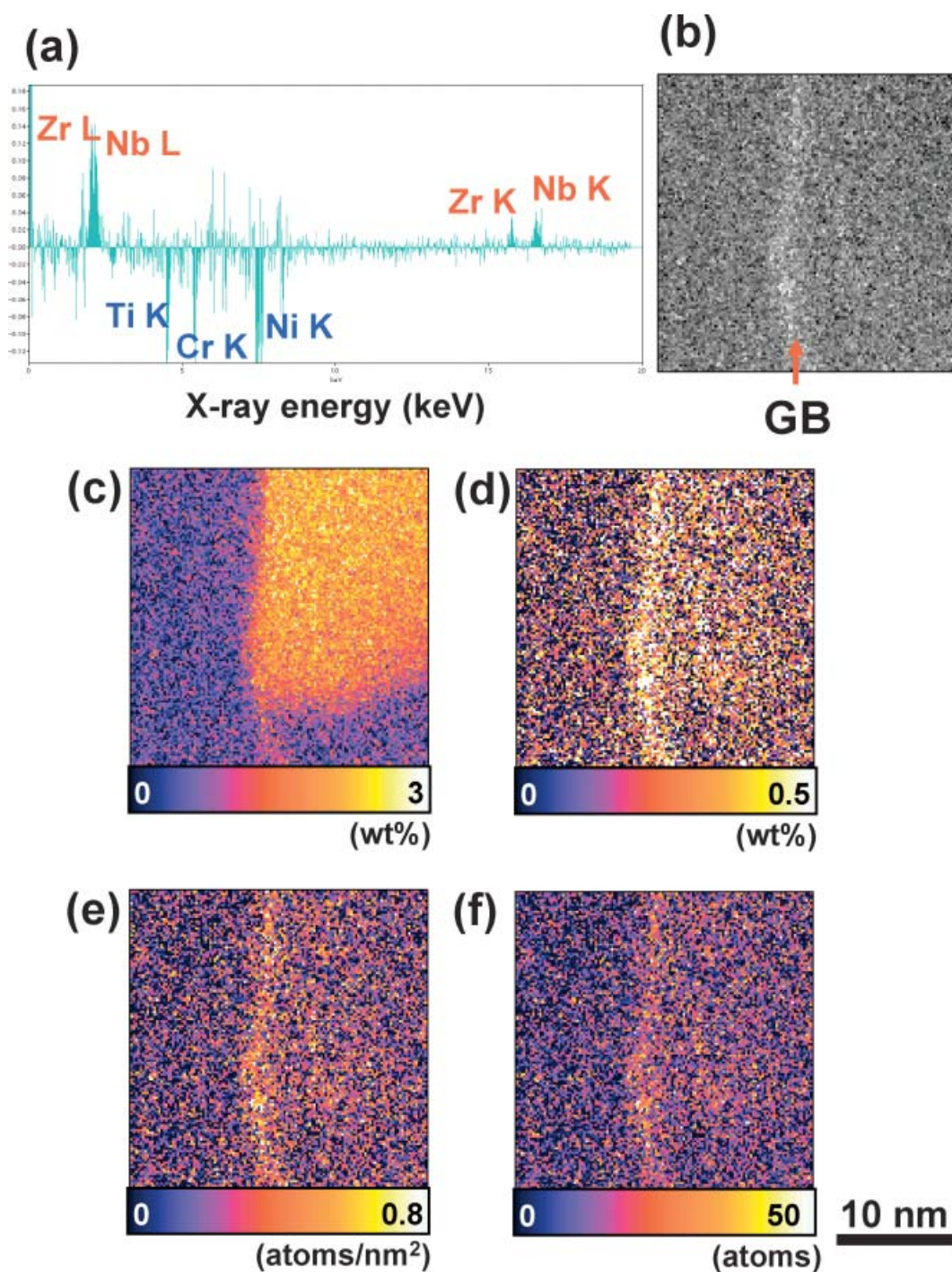


Figure 10. PCA results from the X-ray spectrum image as shown in Figure 8: (a) one of the statistically significant loading spectra and (b) its score image indicate enhancement of X-ray intensities from Zr and Nb at the GB, composition maps of Nb (c) and Zr (d) after the PCA noise-reduction, and maps of the Zr enrichment (e) and the number of Zr atoms (f) determined from the composition and thickness maps.

first indication that atomic-column X-ray analysis and spectrum imaging in a Cs-corrected STEM are at least feasible.

The HAADF-STEM image resolution can be improved using much finer probes obtained by reducing the probe current. According to the plot of the probe size against the

current shown in Figure 6, a 0.3-nm probe that should resolve atomic spacings in lower-index zones in typical metals and alloys can be obtained with a current of 0.2 nA in the Cs-corrected condition. In addition, another interesting fact can be found from Figure 6: The probe sizes remain

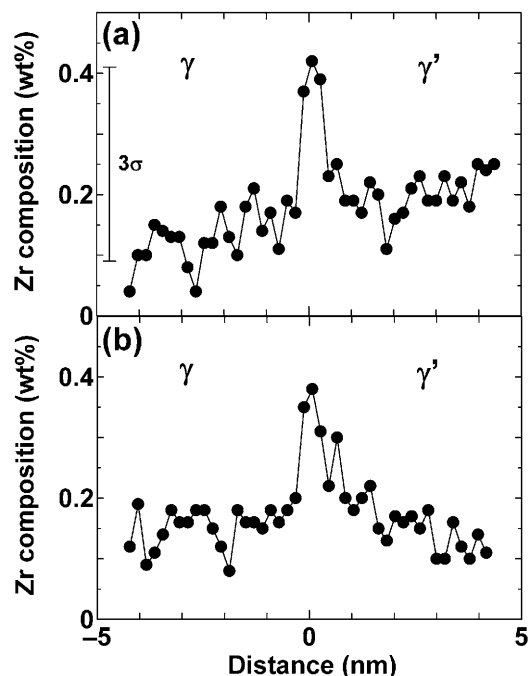


Figure 11. The Zr composition profiles across the γ/γ' interface region (a) and noninterface region (b) on the GB. The error bar indicates a 99% confidence level (3σ). The spatial resolution determined from the profiles is ~ 0.4 – 0.6 nm (FWTM).

almost the same below 0.1 nA in both the uncorrected and Cs-corrected conditions (~ 0.7 nm and ~ 0.25 nm, respectively). The reason the probe sizes are constant below 0.1 nA is because the Gaussian probe sizes become much smaller than the geometrically limited probe sizes (the monochromatic probe sizes in this case) at such lower probe currents. Therefore, 0.1 nA is the maximum applicable probe current without degrading the probe size (and hence image resolution) in this instrument. The maximum applicable current is dependent on the accelerating voltage and the gun brightness (i.e., the electron source), so can be different in other STEMs.

It should be noted that abnormal X-ray emission due to channeling effects may not be avoidable in such atomic-resolving imaging conditions (Bullock et al., 1985). Therefore, for quantification of atomic-column X-ray analyses, appropriate corrections may be required. The channeling correction seems challenging but can be estimated (e.g., Allen et al., 1994; Rossouw et al., 1997).

SUMMARY

In this article, the impact of the Cs-corrector on the spatial resolution and analytical sensitivity of X-ray analysis in an HB 603 STEM were described theoretically and experimentally. As a summary, Figure 13 shows a plot describing the

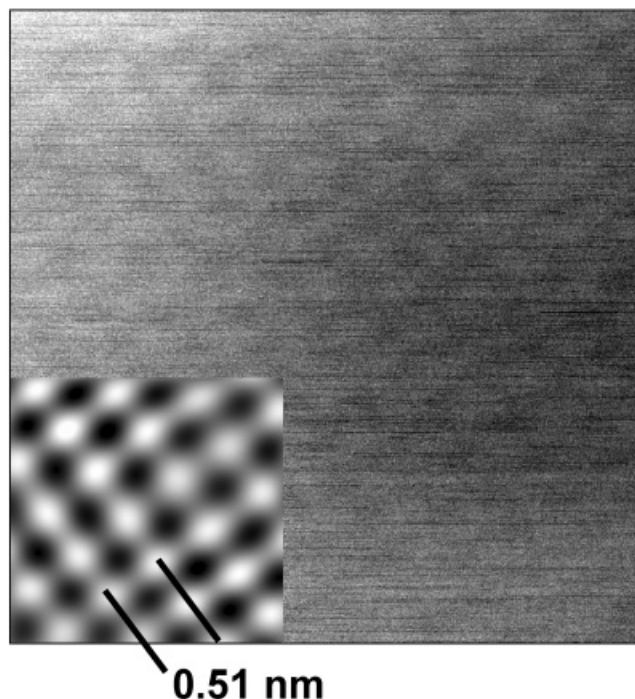
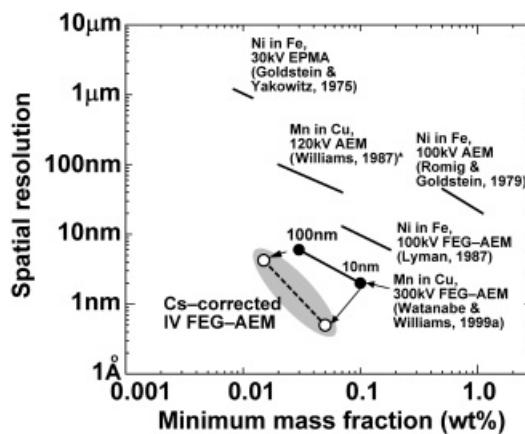


Figure 12. A HAADF-STEM image of ZrO_2 (110) taken in the Cs-corrected HB 603 with a probe current of 0.5 nA. The FFT-filtered image is inserted at the bottom left corner.



*For access to the dataset established by J.R. Michael in 1981, please refer to p. 83 of Williams (1987).

Figure 13. A summary of the X-ray analysis performance of several electron-probe instruments with respect to the spatial resolution and the MMF (modified from Williams et al., 2002). The expected performances for X-ray analysis in the Cs-corrected HB 603 STEM are added as a shadowed area.

relationship between the spatial resolution and the MMF of X-ray analysis in the Cs-corrected STEM, modified from a previous paper (Williams et al., 2002). Using the Cs-corrected HB 603, the spatial resolution may ultimately

reach <0.5 nm for a 10-nm-thick Cu specimen and can be kept <1 nm up to specimen thicknesses of 40 nm with a current of 0.5 nA. The MMF can also be improved due to enhanced characteristic peak intensities because a $10\times$ higher probe current can be obtained in the Cs-corrected HB 603 while keeping the same probe size as in the uncorrected STEM. Installation of the Nion corrector resulted in no degradation of the XEDS performance as measured by the inverse hole count and P/B ratio. Furthermore, the MDM in terms of the number of atoms detected can also be reduced by factors of 2 to 5 because the analyzed volume is significantly reduced as a result of the smaller probe produced by the Cs-corrector. Therefore, the MDM is expected to approach or pass the single-atom level.

The improvement of spatial resolution due to Cs correction was confirmed experimentally from composition profiles across a γ/γ' interphase interface region on a GB in a Ni-base alloy. At the 50-nm-thick region, the measured spatial resolution was ~ 1.8 nm, which agreed with the theoretical estimation. Cosegregation of Zr and Nb was found at both the γ/γ' interface and the noninterphase regions on the GB with the assistance of the PCA technique. This cosegregation of the trace elements Zr and Nb has never been reported in this Ni-base alloy. The maximum composition of Zr is ~ 0.4 wt% on the GB and this signal was generated from only 20–40 Zr atoms. The Zr enrichment at the GB is 2–3 atoms/nm², which is equivalent to 0.12–0.17 of an atomic monolayer. This discovery of the cosegregation is mainly due to the reduction of the analyzed volume by the Cs-corrected probe. Thus, significant improvement in the analytical sensitivity such as the MDM by the Cs-corrector is also demonstrated. The Cs-corrected HB 603 permits X-ray analysis and mapping/spectrum imaging of thin specimens with atomic-scale spatial resolution and single-atom detection capability. This X-ray analytical performance permits the ultimate characterization: detection and identification of individual atoms in materials.

ACKNOWLEDGMENTS

The authors acknowledge the support of the National Science Foundation through grants (DMR-0320906 and DMR-0304738) and of Bechtel Bettis, Inc.

REFERENCES

- ALLEN, L.J., JOSEFSSON, T.W. & ROSSOUW, C.J. (1994). Interaction delocalization in characteristic X-ray emission from light elements. *Ultramicroscopy* **55**, 258–267.
- BATSON, P.E. (1995). Conduction bandstructure in strained silicon by spatially resolved electron energy loss spectroscopy. *Ultramicroscopy* **59**, 63–70.
- BATSON, P.E., DELLBY, N. & KRIVANEK, O.L. (2002). Sub-angstrom resolution using aberration corrected electron optics. *Nature* **418**, 617–620.
- BENNETT, J.C. & EGERTON, R.F. (1995). NiO test specimens for analytical electron microscopy: Round-robin results. *J Microsc Soc Am* **1**, 143–149.
- BROWN, L.M. (1981). Scanning transmission electron microscopy: Microanalysis for the microelectronics age. *J Phys F Metal Phys* **11**, 1–26.
- BROWNING, N.D. & PENNYCOOK, S.J. (1995). Atomic-resolution electron energy-loss spectroscopy in the scanning transmission electron microscopy. *J Microsc* **180**, 230–237.
- BULLOCK, J.F., HUMPHREYS, C.J., MACE, A.J.W., BISHOP, H.E. & TITCHMARSH, J.M. (1985). Crystalline effects in the analysis of semiconductor materials using Auger electrons and X-rays. In *Microscopy in Semiconductor Materials* 1985, Gullis, A.G. & Holt, D.B. (Eds.), pp. 405–410. Bristol: Adam Hilger.
- BURKE, M.G., WATANABE, M., WILLIAMS, D.B. & HYDE, J.M. (2006). Quantitative characterization of nanoprecipitates in irradiated low alloy steels: Advances in the application of FEG-STEM quantitative analysis to real materials. *J Mater Sci* (in press).
- COLLIE, C. & MORY, C. (1984). Quantitative aspects of scanning transmission electron microscopy. In *Quantitative Electron Microscopy*, Chapman, J.N. & Craven, A. (Eds.), p. 149. Glasgow, Scotland: Scottish University Summer School in Physics.
- DELLBY, N., KRIVANEK, O.L., NELLIST, P.D., BATSON, P.E. & LUPINI, A.R. (2001). Progress in aberration-corrected scanning transmission electron microscope. *J Elec Microsc* **50**, 177–185.
- DOIG, P. & FLEWITT, P.E.J. (1982). The detection of monolayer grain boundary segregation in steels using STEM-EDS X-ray microanalysis. *Met Trans A* **13**, 1397–1403.
- EGERTON, R.F. & CHENG, S.C. (1994). Characterization of an analytical electron microscope with a NiO test specimen. *Ultramicroscopy* **55**, 43–54.
- FIORI, C.E., SWYT, C.R. & ELLIS, J.R. (1982). The theoretical characteristic to continuum ratio in energy dispersive analysis in the analytical electron microscope. In *Microbeam Analysis—1982*, Heinrich, K.F.J. (Ed.), pp. 57–71. San Francisco, CA: San Francisco Press.
- GOLDSTEIN, J.I. & YAKOWITZ, H. (1975). *Practical Scanning Electron Microscopy*. New York: Plenum.
- HAIDER, M., ROSE, H., UHLEMANN, S., SCHWAN, E., KABIB, B. & URBAN, K. (1998a). A spherical-aberration-corrected 200 kV transmission electron microscope. *Ultramicroscopy* **75**, 53–60.
- HAIDER, M., UHLEMANN, S., SCHWAN, E., ROSE, H., KABIB, B. & URBAN, K. (1998b). Electron microscopy image enhanced. *Nature* **392**, 768–769.
- HAIDER, M., UHLEMANN, S. & ZACH, J. (2000). Upper limits for the residual aberrations of a high-resolution aberration-corrected STEM. *Ultramicroscopy* **81**, 163–175.
- HAWKES, P.W. & KASPER, E. (1996). Aberration correction. In *Principles of Electron Optics, Vol. 2 Applied Geometrical Optics*, pp. 857–878. London: Academic Press.
- JIA, C.L., LENTZEN, M. & URBAN, K. (2003). Atomic-resolution imaging of oxygen in perovskite ceramics. *Science* **299**, 870–873.
- JOLLIFFE, I.T. (2002). *Principal Component Analysis*, 2nd ed. New York: Springer.
- JOY, D.C. & MAHER, D.M. (1977). Sensitivity limits for thin specimen X-ray analysis. In *Scanning Electron Microscopy—1977*, Johari, O. (Ed.), vol. 1, pp. 325–334. Chicago: IITRI.

- KEAST, V.J. & WILLIAMS, D.B. (1999). Quantitative compositional mapping of Bi segregation to grain boundaries. *Acta Mater* **47**, 3999–4008.
- KRIVANEK, O.L., DELLBY, N. & LUPINI, A.R. (1999). Toward sub-Å electron beams. *Ultramicroscopy* **78**, 1–11.
- KRIVANEK, O.L., NELLIST, P.D., DELLBY, N., MURFITT, M.F. & SZILAGYI, Z. (2003). Toward sub-0.5 Å electron beams. *Ultramicroscopy* **96**, 229–237.
- LYMAN, C.E. (1987). Prospects for analytical electron microscopy by X-ray emission spectroscopy. In “Physical Aspects of Microscopic Characterization of Materials,” Kirschner, J., Murata, K. & Venables, J.A. (Eds.), *Scanning Microscopy International*, Suppl. 1, pp. 123–134.
- LYMAN, C.E. & ACKLAND, D.W. (1991). The standard hole count test: A progress report. In *Microbeam Analysis—1991*, Howitt, D.G. (Ed.), pp. 720–721. San Francisco, CA: San Francisco Press.
- LYMAN, C.E., GOLDSTEIN, J.I., WILLIAMS, D.B., ACKLAND, D.W., VON HARRACH, H.S., NICHOLLS, A.W. & STATHAM, P.J. (1994). High performance X-ray detection in a new analytical electron microscope. *J Microsc* **176**, 85–98.
- MALINOWSKI, E.R. (2002) *Factor Analysis in Chemistry*, 3rd ed. New York: Wiley.
- MICHAEL, J.R., WILLIAMS, D.B., KLEIN, C. & AYER, R. (1990). The measurement and calculation of the X-ray spatial resolution obtained in the analytical electron microscope. *J Microsc* **160**, 41–53.
- MILLER, M.K. & BURKE, M.G. (1993). An APFIM/AEM characterization of alloy X-750. *Appl Surf Sci* **67**, 292–298.
- MORY, C., TENCE, M. & COLLIEX, C. (1985). Theoretical study of the characteristics of the probe for a STEM with a field emission gun. *J Microsc Spectrosc Electron* **10**, 381–387.
- NELLIST, P.D., CHISHOLM, M.F., DELLBY, N., KRIVANEK, O.L., MURFITT, M.F., SZILAGYI, Z.S., LUPINI, A.R., BORISEVICH, A., SIDES, W.H., JR. & PENNYCOOK, S.J. (2004). Direct sub-angstrom imaging of a crystal lattice. *Science* **305**, 1741.
- NEWBURY, D.E. (2005). X-ray spectrometry and spectrum image mapping at output count rates above 100 kHz with a silicon drift detector on a scanning electron microscope. *Scanning* **27**, 227–239.
- PENNYCOOK, S.J. (1982). High resolution electron microscopy and microanalysis. *Contemp Phys* **23**, 371–400.
- REED, S.J.B. (1982). The single-scattering model and spatial resolution in X-ray analysis of thin foils. *Ultramicroscopy* **7**, 405–410.
- RODRÍGUEZ-GONZÁLEZ, B., BURROWS, A., WATANABE, M., KIELY, C.J. & LIZ MARZÁN, L.M. (2005). Multishell bimetallic AuAg nanoparticles: Synthesis, structure and optical properties. *J Mater Chem* **15**, 1755–1759.
- ROMIG, A.D., JR. & GOLDSTEIN, J.I. (1979). Detectability limit and spatial resolution in STEM X-ray analysis: Application to Fe-Ni. In *Microbeam Analysis—1979*, Newbury, D.E. (Ed.), pp. 124–128. San Francisco, CA: San Francisco Press.
- ROSE, H. (1990). Outline of a spherically corrected semiplanatic medium-voltage transmission electron microscope. *Optik* **95**, 19–24.
- ROSSOUW, C.J., FORWOOD, C.T., GIBSON, M.A. & MILLER, P.R. (1997). Generation and absorption of characteristic X-rays under dynamical electron diffraction conditions. *Micron* **28**, 125–137.
- SAWADA, H., TOMITA, T., NARUSE, M., HONDA, T., HAMBRIDGE, P., HARTEL, P., HAIDER, M., HETHERINGTON, C., DOOLE, R., KIRKLAND, A., HUTCHISON, J., TITCHMARSH, J. & COCKAYNE, D. (2005). Experimental evaluation of a spherical aberration-corrected TEM and STEM. *J Electron Microsc* **54**, 119–121.
- VAN CAPPELLAN, E. & SCHMITZ, A. (1992). A simple spot-size versus pixel-size criterion for X-ray microanalysis of thin foils. *Ultramicroscopy* **41**, 193–199.
- VARELA, M., LUPINI, A.R., VAN BENTHEM, K., BORISEVICH, A.Y., CHISHOLM, M.F., SHIBATA, N., ABE, E. & PENNYCOOK, S.J. (2005). Materials characterization in the aberration-corrected scanning transmission electron microscope. *Annu Rev Mater Res* **35**, 539–569.
- WATANABE, M. & WILLIAMS, D.B. (1999a). Atomic-level detection by X-ray microanalysis in the analytical electron microscope. *Ultramicroscopy* **78**, 89–101.
- WATANABE, M. & WILLIAMS, D.B. (1999b). The new form of the ζ -factor method for quantitative microanalysis in AEM-XEDS and its evaluation. *Microsc Microanal* **5**(Suppl. 2), 88–89.
- WATANABE, M. & WILLIAMS, D.B. (2003). Quantification of elemental segregation to lath and grain boundaries in low-alloy steel by STEM X-ray mapping combined with the ζ -factor method. *Z Metallk* **94**, 307–316.
- WATANABE, M. & WILLIAMS, D.B. (2006). The quantitative analysis of thin specimens: A review of progress from the Cliff-Lorimer to the new ζ -factor methods. *J Microsc* **221**, 89–109.
- WILLIAMS, D.B. (1987). *Practical Analytical Electron Microscopy in Materials Science*, 2nd ed. Mahwah, NJ: Philips Electron Optics Publishing Group.
- WILLIAMS, D.B., MICHAEL, J.R., GOLDSTEIN, J.I. & ROMIG, A.D., JR. (1992). Definition of the spatial resolution in X-ray microanalysis in thin foils. *Ultramicroscopy* **47**, 121–132.
- WILLIAMS, D.B., PAPWORTH, A.J. & WATANABE, M. (2002). High resolution X-ray mapping in the STEM. *J Electron Microsc* **51S**, S113–S126.
- ZACH, J. & HAIDER, M. (1995). Aberration correction in a low voltage SEM by a multipole corrector. *Nucl Instrum Methods Phys Res A* **363**, 316–325.
- ZALUZEC, N.J. (2004). XEDS systems for the next generation analytical electron microscope. *Microsc Microanal* **10**(Suppl. 2), 122–123.
- ZIEBOLD, T.O. (1967). Precision and sensitivity in electron microprobe analysis. *Anal Chem* **39**, 858–861.